# On the sources of cyclic loads in horizontal-axis wind turbines: The role of blade-section misalignment

Alejandro D. Otero [a, b, c, *], Fernando L. Ponta [c]

[a] Universidad de Buenos Aires, Facultad de Ingeniería, Buenos Aires, Argentina
[b] CSC-CONICET, Buenos Aires, Argentina
[c] Department of Mechanical Engineering - Engineering Mechanics, Michigan Technological University, Houghton, MI 49931, United States

## ARTICLE INFO

## ABSTRACT

In this paper we investigate the sources of cyclic loads affecting the structural solicitation and power production in Horizontal Axis Wind Turbines, in particular the role of blade-section misalignment. These loads could become determinant in future designs of extra-large turbines, limiting lifespan due to fatigue of structural and mechanical components. Gravity loads would also become more significant in future up-scaled machines due to the square-cube law relation between energy capture and rotor mass.

We identify the different constructive factors and physical mechanisms which constitute the sources of the cyclic loads on the rotor, and present a methodology to analyze the contribution of each one of them. We propose six hypothetical scenarios to illustrate the individual effect of each of the aforementioned sources on the aerodynamic and structural variables that characterize the operational state of the turbine.

We analyze the evolution of aerodynamic variables which characterize rotor interference and its relation with the angle of attack on the blade sections. Structural variables are also analyzed, showing the contribution of both aerodynamic and gravity loads, inducing out-of-plane bending and torsional oscillations, and how these could be activated by bend-twist coupling on the blade structural response.

© 2017 Elsevier Ltd. All rights reserved.

## 1. Introduction

Wind turbines function in the presence of fluctuations that can be detected in macroscopic variables of interest like power and thrust. Although a vast amount of research on fluctuating loads on wind turbines focus on turbulent causes [1–5], fluctuations can be observed even for spatially and temporal constant wind profile due to turbine design and configuration. These fluctuations are different from the essentially chaotic fluctuations resulting from wind variation (e.g. atmospheric boundary layer wind profile, gusts, turbulence) in that they are typically periodic. In this paper we investigate the sources of cyclic loads affecting the structural solicitation and power production in Horizontal Axis Wind Turbines (HAWTs). In particular, the role of blade-section misalignment, that is, changes of attitude of the airfoil sections due to instantaneous deformation, plus other factors like yaw, tilt, pitch, coning and

initial twist and bending curvature of the blade design. These factors would likely become even more important in the future. For example, more flexible blades in future turbines will deform more and may require tilt to be increased in order to avoid tower collision, both factors will increase airfoil-section misalignment and produce higher cyclic loads.

These loads could become determinant in future extremely large turbines limiting lifespan due to fatigue of structural and mechanical components or producing catastrophic failure after triggering resonance or unstable behavior at some particular frequency. According to Bir and Jonkman [6] future turbine design will be prone to be conditioned by stability in contrast to the loads-driven design of the past. Holierhoek [7] thoroughly reviewed possible aeroelastic blade instabilities in present and future larger turbines. An example of this are the results obtained at Sandia National Laboratories by the 100 m blade project [8–10] where an upscaled turbine blade is analyzed. With the increased blade length there has been an increase in the cyclic edgewise loading and an associated increase in trailing-edge fatigue issues. During the whole life span of a wind turbine the revolution count can be typically well over 10 million revolutions [11,12] which is the

* Corresponding author. CSC − CONICET, Godoy Cruz 2390, C1425FQD, Buenos Aires, Argentina.
E-mail address: alejandro.otero@csc.conicet.gov.ar (A.D. Otero).

number of cycles usually used to define the endurance limit in fatigue calculations for materials where it can be defined, so results need to be analyzed from a fatigue point of view.

The issue of cyclic non stochastic loading is barely studied in the literature. Zalkind and Pao [13] studied the fatigue loading effects of using an intentional yaw misalignment to redirect wakes in order to increase overall plant power capture. They focus on the effect of cyclic loads originated in the yaw misalignment used to redirect turbine wakes in order to increase overall plant power capture and compare two control strategies: one collective and one individual. Kim et al. [14] analyzed the effect of bend-twist coupling on blade root fatigue loads and blade tip clearance through a parametric study in terms of the coupling magnitude.

The detailed study of complex aeroelastic phenomena in wind turbine blades has required the advancement of combined aerodynamic and structural codes during the past decade [15]. Gebhardt and Roccia [16] developed an aeroelastic code based on a segregated structural formulation and a vortex sheet aerodynamic model capable of capturing nonlinear effects such as flutter, etc. Mo et al. [17] coupled a multi-body system structural model with a modified Blade Element Momentum (BEM) model that includes blade vibration and torsional deformation, shown to have significant effects on aerodynamic loads. In addition, the dynamic stall model increases fluctuation of blade aerodynamic loads, affecting the blade fatigue load spectrum and the fatigue life design. Wang et al. [18] presented a nonlinear aeroelastic model for large wind turbine blades developed by combining a BEM model and a mixed-form formulation of geometrically exact beam theory which was applied to aeroelastic modeling of the parked WindPACT 1.5 MW turbine [19] comparing results to the classic FAST code [20]. Meng et al. [21] proposed an elastic actuator line model, which is the combination of the actuator line wake model and a finite difference structural model. The wake interaction involving two staggered HAWTs was carried out, showing that the downstream wind turbine experiences a wake-induced fatigue increase.

Future scaling of wind turbines faces the limit imposed by the so-called *square-cube law* [22]. This refers to the fact that turbine power grows with the square of the size due to its dependence on the rotor area while mass and weight, associated with the volume, tend to grow with the cube of the size of the rotor if geometric similarity is maintained when scaling. Thus, stresses due to blade weight scale linearly with the size of the rotor unlike other stresses (e.g. stresses due to aerodynamic or centrifugal forces) that remain constant as rotor size increases. As a consequence, the wind turbine industry will need to find the way to grow blade size without increasing the weight with the cubical scale of the size. The need for a new generation of what could be called Ultra Light Blades (ULBs) will also be imposed by economical reasons. If the size of the turbines (rotor radius) is to be scaled by a certain factor, the power of that turbine is expected to scale with the square of that factor but the mass will scale with its cube, increasing the share of rotor cost on the specific cost of the turbine. In order to keep a favorable tendency in terms of economies of scale, again, there will be a need for reducing blade mass to keep the proportional cost of materials, labor, transport and assembly within feasible limits. The level of mass reduction required by economical considerations will be determined by a combination of economies of scale of all the other items involved in wind turbine manufacture and installation.

Fig. 1 shows, in the left column, the torque and thrust time evolution for a the 3-bladed rotor of the NREL 5 MW reference wind turbine (RWT) as defined by Jonkman et al. [23] working at nominal wind speed with a constant flat wind profile. These basic test conditions are shown as a reference to provide a starting point to correctly asses the effect of other off-design conditions that we shall analyze below. The resulting curves are periodic with a frequency triple of the rotor, but their shape is not pure sinusoidal, which indicates the presence of higher frequency modes of oscillatory deformation.

As stated above, future ULBs will tend to be more flexible due to the reduction of their mass to avoid the consequences of the square-cube law. To analyze the impact of the ULB philosophy in future blade design we devised a test-case using a hypothetical *light blade* with the same geometry of the RWT's but with a reduction of 10% in weight on its structural fiber-reinforced layers.

Fig. 1 shows a comparison of the time evolution of rotor power and thrust for the light-blade test case and the standard blade of the RTW. The light-blade curves show a higher complexity than those of the standard blade, with an increasing presence of higher frequency modes and a reduction of the mean values for both parameters.

In Section 2 of the present work, we shall identify the different physical mechanisms which constitute the sources of the cyclic loads in the observed response, and in Section 3, we will present the methodology employed to analyze the contribution of each one of them, and the role of misalignment. In Section 4, we shall present six cases to illustrate the individual effect of each of the aforementioned sources on the aerodynamic and structural variables that characterize the operational state of the turbine, and analyze their effect on fatigue. Finally, we shall draw conclusions about these future aspects of ULB turbine rotors.

## 2. Sources of cyclic loads

The sources of cyclic loads can be grouped in the following categories according to their nature:

**Aerodynamic interference** of the rotor may vary with time, which results in fluctuations of wind velocity at the rotor plane in both, magnitude and direction, along the turning cycle. This is an instantaneous aerodynamic manifestation associated with the wind velocity deficit induced by the process of power extraction exerted by the blades on the wind flow at each position along the blade span.

**Constructive features** which are specific for a particular turbine design could induce variations on blade loads. There are several design parameters which break symmetry around the rotor's axis, and give raise to unsteady conditions, namely:

- Tilt angle
- Cone angle
- Blade twist, pre-bending and sweptback curvatures

**Turbine mechanisms** make the interaction between wind and blades change at different working conditions. The magnitudes associated to the principal mechanisms that result in non steady situations can be divided into:

**Geometric**: referring to quantities that affect the geometric setting of the attitude of the blade airfoil section. The main geometric magnitudes are:

- Azimuth angle, which relates to the instantaneous position of the blade in its rotation around the main shaft.
- Yaw angle, which relates to the misalignment between wind direction and nacelle axis.
- Pitch angle, if the blade was actuated to compensate for cyclical events.

**Kinematic**: meaning quantities that affect the composition of the velocity vectors incident on the different airfoil sections along the span. The chief kinematic magnitude is:
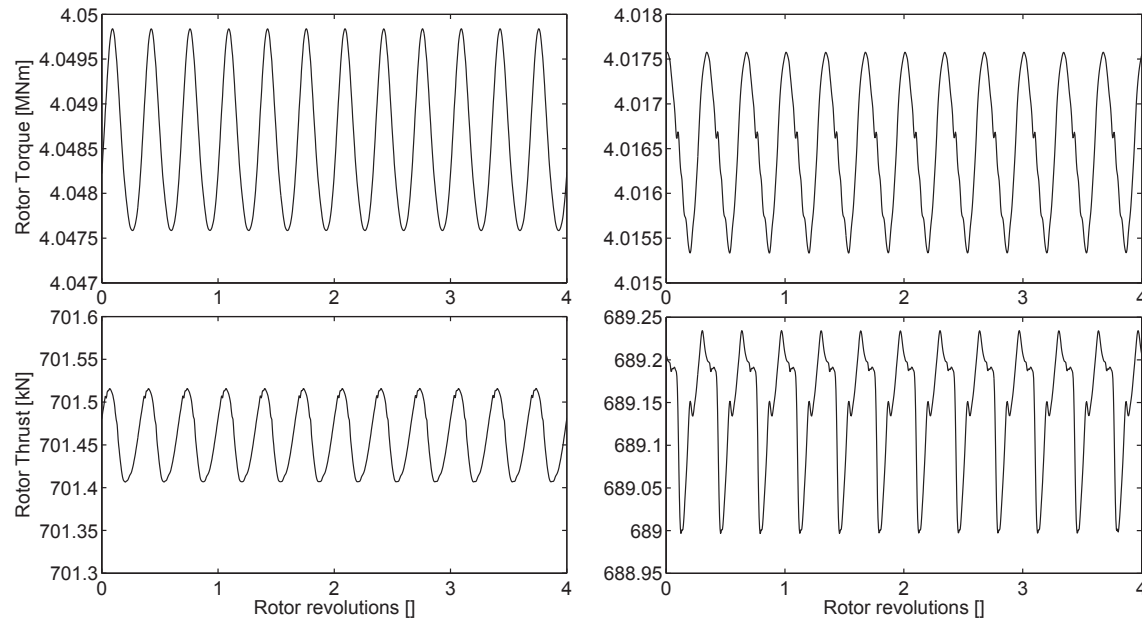
**Fig. 1.** Time evolution of rotor torque and thrust for a 3-bladed RWT at nominal operational conditions during 4 cycles. Left column correspond to a standard NREL 5 MW RWT and right column to the light-blade test case.

- Tangential velocity of each blade section with respect to the plane of rotation, which is composed with the local wind to give the incident velocity. It is given by the rotational velocity of the blade multiplied by the instantaneous radial distance of the blade section to the main shaft. This radial distance will vary dynamically with instantaneous deformation.

**Deformation** of turbine components (mainly blades and tower) also affects the loading situation in two senses in a similar way as the mechanisms:

**Geometric**: deformation that change the aerodynamic attitude of each airfoil section along the span. It can be divided in terms of the type of deformation:

- Torsional, mainly affecting the attitude of the airfoil in the plain of the airfoil section itself (and thus, the angle of attack)
- Flexural, which affects mainly the instantaneous alignment of the airfoil section with respect to its original alignment in a plane normal to the blade design axis.

**Kinematic**: involves the velocity of blade sections due to vibrational deformation which, when composed with the tangential velocities and the local wind, determines the total incident velocities on the airfoil sections.

Some of these effects act independently, some act in a coupled manner and some are compounded by the action of an additional effect like gravity which, by affecting the deformation, also affects the geometry modifying the aerodynamic loads. The block diagram of Fig. 2 schematically summarizes how the above-mentioned effects relate each other and how they finally affect the aerodynamic forces through the apparent wind incident on the airfoil sections. Relations among the different factors will become clearer in the next section, where we describe the fundamentals of the aero-elasto-inertial model that was used to conduct the simulations for the rotor behavior. The logic of this model closely resembles the sequence of Fig. 2 block diagram.

## 3. Methodology

### 3.1. Aero-elasto-inertial modeling of wind turbines

We model the fluid−structure interaction dynamics of the wind turbine rotor by means of the *DRD-BEM* aerodynamic model described by Ponta et al. [24] coupled with the structural model presented by Otero and Ponta [25]. Early versions of these two models, were previously used to analyze the NREL-RWT with standard and adaptive blades by Otero et al. [26] and Lago et al. [27]. This modeling tool is able to take into account all the features related to the physical mechanisms presented in the previous section, and also has the capacity of turning off some of them selectively to evaluate their incidence on the overall behavior. It has unique capabilities to study this problem compared with other models presented in the literature that share a similar approach. As stated in Zhang and Huang [28], this is a crucial aspect because, with the increasing size of turbines and much more flexible blades, the assumptions of small deformation and displacement for linearization are not valid. Modeling the multi-megawatt wind turbines nonlinear effects, e.g. the nonlinear effects due to large blade deflection, have to be accounted for. This had prompted upgrades to classical models like the FAST Aerodyn [20] where more advanced structural models were introduced by Wang et al. [29].

A key feature of the DRD-BEM that differs from previous models based on the BEM theory [17,18,20,30,31] is that it includes all the aforementioned geometrical and structural nonlinear effects associated to the dynamic deformation of composite blades of complex geometry. In the DRD-BEM, the velocities and forces involved in the aerodynamic computations are transformed by a series of orthogonal matrices acting as linear operators. These matrices represent the changes of attitude of the airfoil sections due to instantaneous deformation, plus other factors like yaw, tilt, pitch, coning and initial twist and bending curvature of the blade design.

In this section we will briefly review the fundamental aspects of the DRD-BEM procedure, referring the reader to Ponta et al. [24] and Otero and Ponta [25] for more details. We start by considering the velocity vector of the flow passing through an annular
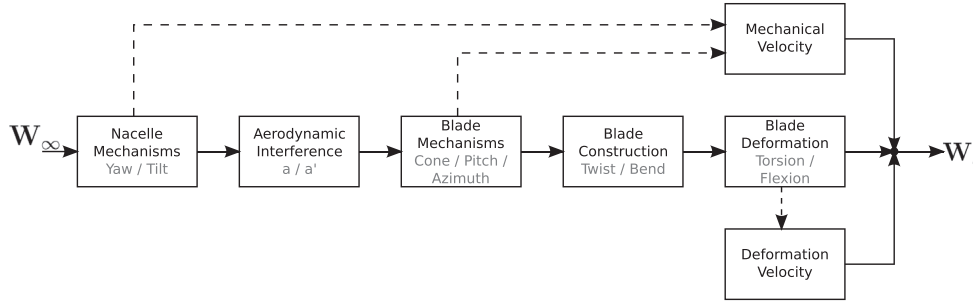
**Fig. 2.** Block diagram with a conceptual interpretation of the interaction among different sources of cyclical loads.

actuator aligned with the hub coordinate system $h$. The components of this velocity vector are affected by the axial induction factor $a$ (i.e. normal to the annular actuator) and the tangential induction factor $a'$, representing respectively the axial velocity deficit and the increase in tangential velocity across the actuator. These two factors are obtained by an optimized iterative solution process described in Ponta et al. [24]. Then,

$$\mathbf{W}_h = \begin{bmatrix} W_{\infty h_x}(1-a) \\ W_{\infty h_y} + \Omega\, r_h a' \\ W_{\infty h_z} \end{bmatrix}, \tag{1}$$

is the velocity vector of the wind going through the annular actuator. $\mathbf{W}_{\infty h}$ is the undisturbed wind velocity field referred to the hub coordinate system, $\Omega$ is the angular velocity of the rotor, and $r_h$ is the instantaneous radial distance.

For the cases of rotors with tilt, and/or in the presence of changes in yaw angle and wind direction, the three-dimensional nature of $\mathbf{W}_{\infty h}$ will take those effects into account. In order to do this, we use a set of orthogonal matrices to transform the wind velocity defined in a coordinate system aligned with the wind itself, into the hub coordinate system, $\mathbf{W}_{\infty h} = \mathbf{C}_{\theta_{az}}\mathbf{C}_{\theta_{tlt}}\mathbf{C}_{\Delta\theta_{yaw}}\mathbf{W}_{\infty wind}$.

Next, the velocity vector is projected on the blade section coordinate system. These coordinate systems are shown in Fig. 3. Thus, $\mathbf{W}_h$ will be projected going through several coordinate systems, from the hub to the system aligned with the blade section. After all these transformations, the velocity vector $\mathbf{W}_h$ is expressed into the coordinate system of the blade section, and then we add the blade section vibrational velocities $\mathbf{v}_{str}$ coming from the structural model. We also add the velocity components $\mathbf{v}_{mech}$,

associated with the motion of the blade section due to the combined action of mechanical devices (like yaw, pitch, and azimuthal rotation around the main shaft), expressed in the coordinate systems of the blade section $l$. Thus, the expression for the wind velocity relative to the blade section, $\mathbf{W}_l$, results:

$$\mathbf{W}_l = \left( \mathbf{C}_{lL}\mathbf{C}_{Lb}\mathbf{C}_{\theta_p}\mathbf{C}_{\theta_{cn}}\mathbf{W}_h \right) + \mathbf{v}_{str} + \mathbf{v}_{mech}. \tag{2}$$

The coning transformation matrix $\mathbf{C}_{\theta_{cn}}$ is a linear operator taking into account the coning angle for the rotor and is characterized by a rotation around the second axis of the hub coordinate system (Fig. 3 (a)). Similarly, the pitching transformation matrix $\mathbf{C}_{\theta_p}$, is related to a rotation around the pitch axis of the blade, which is the third axis of the coordinate system resulting from the previous coning transformation (Fig. 3 (b)).

The orthogonal matrix $\mathbf{C}_{Lb}$ is based on the geometrical alignment of the blade sections along the span defined at the time when the blade was designed and manufactured (Fig. 3 (c)). It takes into account the fact that the blade could have pre-conformed curvatures along its longitudinal axis (i.e. the design blade axis is no longer rectilinear and the coordinate systems of different blade sections along the reference line are no longer aligned with the third axis of the blade root system $b$). The intrinsic system $L$ is defined aligned to the blade sections in the chord-normal, chord-wise, and span-wise directions. Thus, the abovementioned curvatures can reflect either an initial twist along the longitudinal axis or a combination of twist plus pre-bending on the other two axes (i.e. coning-wise/sweeping-wise). The orthogonal matrix $\mathbf{C}_{lL}$, is the one provided by the solution of the kinematic equations on the structural model (as explained in Ponta et al. [24]), which transforms
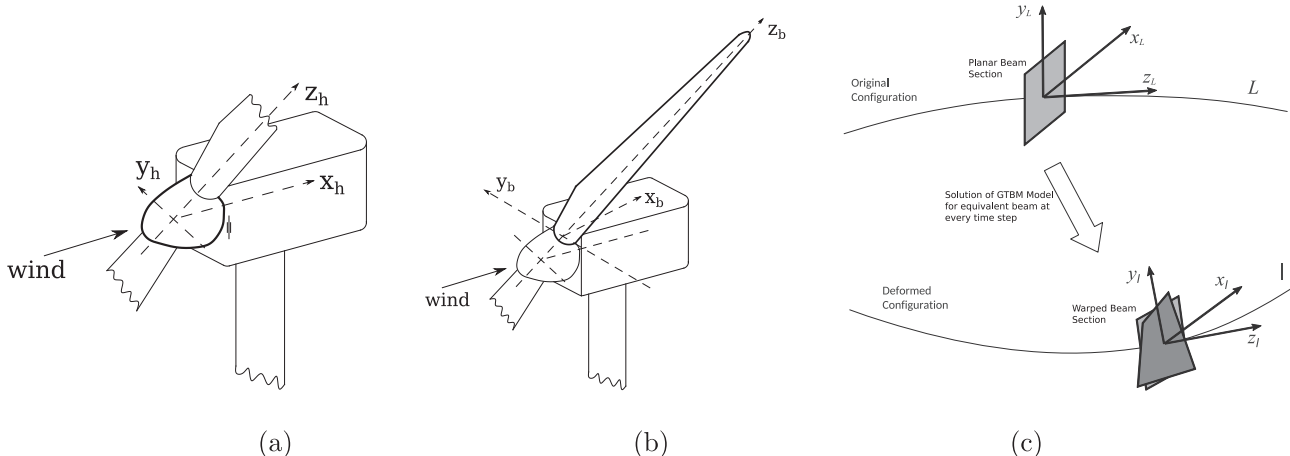


**Fig. 3.** Coordinate systems associated with the rotor hub (a), blade root (b), and blade section in undeformed and deformed configuration (c).

vectors from system $L$ to system $l$ (Fig. 3 (c)).

With the magnitude of the wind velocity projection onto the plane of the blade section, $W_{rel} = \sqrt{W_{l_x}^2 + W_{l_y}^2}$, and its angle of attack $\alpha$, the aerodynamic lift and drag forces per unit length of span are computed:

$$dF_{lift} = \frac{1}{2}\rho\, C_l\, W_{rel}^2\, c \tag{3}$$

$$dF_{drag} = \frac{1}{2}\rho\, C_d\, W_{rel}^2\, c, \tag{4}$$

where $C_l$ and $C_d$ are the lift and drag coefficients computed at the instantaneous angle of attack $\alpha$, $\rho$ is the air density, and $c$ is the chord length of the airfoil section. The total aerodynamic load acting on the blade element of length $\delta l$ relative to the wind direction has components corresponding to the lift and drag forces and is given by

$$\delta\mathbf{F}_{rel} = \begin{bmatrix} dF_{lift} \\ dF_{drag} \\ 0 \end{bmatrix} \delta l. \tag{5}$$

The aerodynamic moment on the airfoil section per unit span-length, which acts around the first axis of $l$, is also considered. It is computed as $dM_{aer} = \frac{1}{2}\rho\, C_m\, W_{rel}^2\, c^2$. Our model also considers the three-dimensional contribution of the gravitational action to the distributed forces and moments along the span. It is computed considering the instantaneous position and attitude of each blade section. Fig. 4 shows a flowchart of the seven fundamental steps of the algorithmic sequence of the DRD-BEM including the iterative
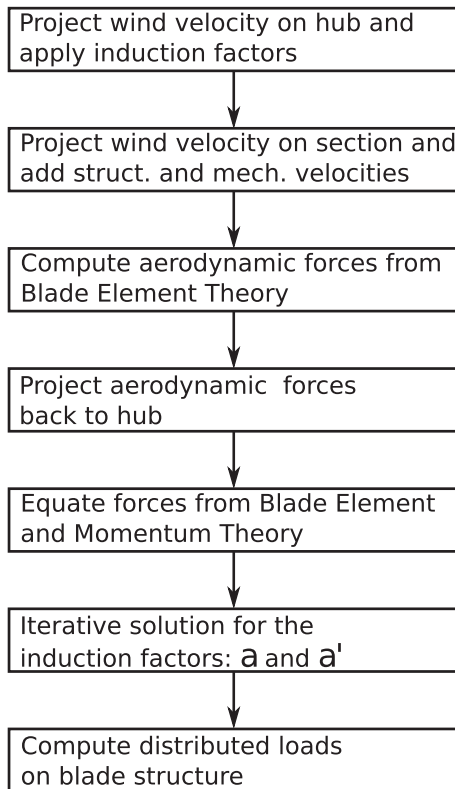
| Project wind velocity on hub and apply induction factors |
| --- |
| ↓ |
| Project wind velocity on section and add struct. and mech. velocities |
| ↓ |
| Compute aerodynamic forces from Blade Element Theory |
| ↓ |
| Project aerodynamic forces back to hub |
| ↓ |
| Equate forces from Blade Element and Momentum Theory |
| ↓ |
| Iterative solution for the induction factors: a and a' |
| ↓ |
| Compute distributed loads on blade structure |

**Fig. 4.** Flowchart of the seven fundamental steps of the algorithmic sequence of the DRD-BEM (see Ponta et al. [24]) including the iterative solution for the interference factors and the computation of aerodynamic forces in each blade section.

solution for the interference factors and the computation of aerodynamic forces in each blade section [24].

### 3.2. The role of misalignment

We will further analyze the origin of different phenomena that cause aerodynamic load variation by a qualitative decomposition of the angle of attack. We start by examining Equation (2), and considering the rotation corresponding to each orthogonal matrix in the plane of the section, we define the following angles:

- $\phi_{h_z}$: angle of incident wind on the rotor plane, i.e. the angle between the relative wind $\mathbf{W}_h$ and the plane of the rotor. This is mainly influenced by the yaw and tilt of the rotor and the rotor's aerodynamic interference on the wind free stream. Its relation with $\mathbf{W}_\infty$ and the interference factors is shown in Fig. 5(a).
- $\alpha$: angle of attack (AoA), i.e. the angle between the apparent wind vector $\mathbf{W}_l$ as defined in Section 3.1, projected in the plane of the airfoil section at a certain position along the span, according to Fig. 5(b).
- $\varphi$: angle of the total apparent wind on the blade section; i.e. the angle between the direction of rotation of the blade section, and the direction of the total incoming wind, which includes the effects of the yaw, tilt, and aerodynamic interference of the rotor, plus the contribution to the incident wind by the motion of the blade section due to structural vibration, $\mathbf{v}_{str}$, and the combined action of mechanical devices, $\mathbf{v}_{mech}$ (mainly, the tangential velocity of the blade section on its rotation around the main shaft).
- $\beta$: section pitch angle. This is a constructive and/or operational characteristic of the rotor, and includes the effect of rotor coning, blade pitch, and twist and curvature of the undeformed blade given by matrices $\mathbf{C}_{Lb}$, $\mathbf{C}_{\theta_p}$ and $\mathbf{C}_{\theta_{cn}}$.
- $\theta_{tor}$: angle of dynamic deformation. Angle change due to twist deformation of the blade, this is mainly given by the component of the angle of deformation co-linear with the blade axis coming from matrix $\mathbf{C}_{lL}$. This item could be high in case of low blade torsion stiffness.

Analyzing the effects described in Section 2 in terms of Equation (2) on a blade section at a certain position along the span, as depicted in Fig. 5(b), the above mentioned angles relate one another according to:

$$\alpha = \varphi - \beta - \theta_{tor}. \tag{6}$$

Equation (6) can be interpreted as an *angular representation* of Equation (2) when projected on the blade axis passing through each section.

We also define the out-of-plane angle (OoP) which represents the angle between the apparent wind vector $\mathbf{W}_l$ and the plane of the airfoil section at a certain position along the span. This is due to a combination of constructive and/or operational characteristics of the rotor plus the angle change due to bending deformation of the blade, i.e. all rotation on the section coming from matrix $\mathbf{C}_{lL}$ not considered by $\theta_{tor}$. This last item could be high in case of low blade bending stiffness.

### 4. Numerical results and analysis

In order to analyze the different factors giving rise to cyclic loading we ran a set of numerical experiments on an NREL 5 MW-RWT rotor as defined by Jonkman et al. [23] by means of the aero-elasto-inertial model described in Section 3.1. The simulations were carried out imposing a uniform wind profile of 11.4 m/s with the
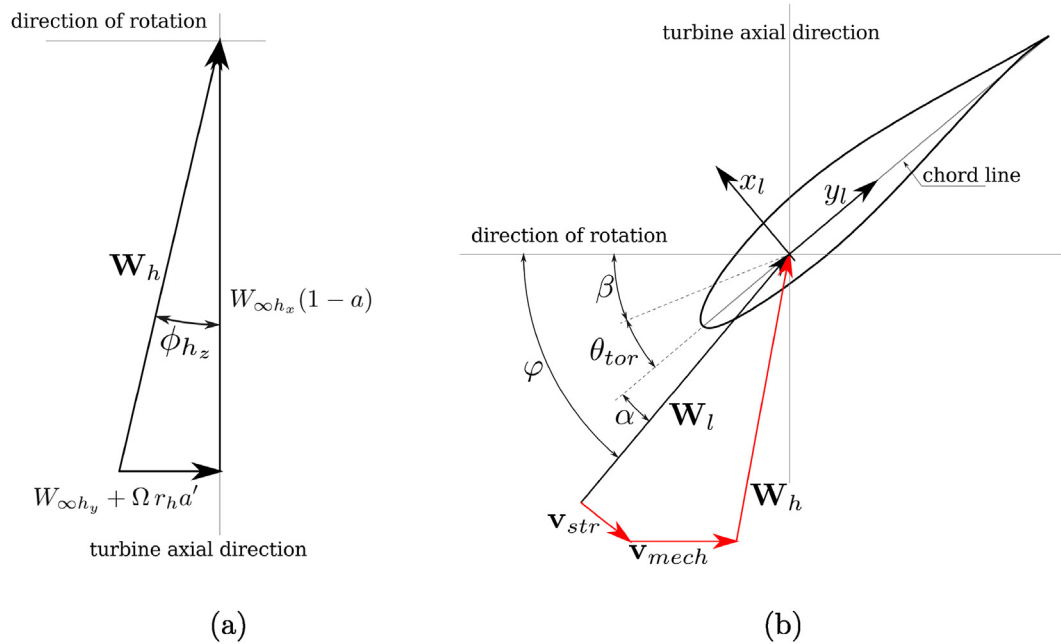
**Fig. 5.** Schematics of different factors affecting the apparent wind in the blade section: (a) composition of the incident wind vector $\mathbf{W}_h$ in the plane of the rotor, and (b) composition of the apparent wind vector $\mathbf{W}_l$ according to Equation (2).

rotor turning at 12.1 rpm, which correspond to nominal operational conditions of the NREL 5 MW-RTW. These conditions impose pure periodic loading on the rotor blades in contrast to other non-periodic effects that can result from considering effects in the atmospheric boundary layer such as wind profile, turbulence or gusts. The level of description attained by the DRD-BEM allow us to consider every and all the effects mentioned in Section 2. In order to elucidate the relative importance of each of them, they can be selectively switched on or off. Deformation effects can be switched off by simulating a turbine with what we call *hyper-stiff* blade, which is a hypothetical blade with the same aerodynamic geometry of the standard, but whose structural stiffness coefficients are set to be $10^3$ times higher than those of the standard one. We run our experiments for more than 70 rotor revolutions, to avoid transient effects and ensure a regular regime operation.

Among all the possible scenarios that could be explored, we selected six, which in our opinion will provide the maximum insight in terms of characterizing the rotor behavior. This set of scenarios allow us to better draw conclusions about the relevance of each factor and their interrelation. The parameters to be switched on, off, and/or combined in these study cases are:

- cone and tilt as representative of constructive features defining the geometry of the rotor, respectively producing symmetric and asymmetric effects with respect to the rotor's axis;
- deformation of the blade, which includes both, geometric and kinematic effects, switched off by means of using the *hyper-stiff* blade explained before;
- gravity loads switched on or off.

We adopted a short-hand nomenclature to identify the six proposed scenarios, namely:

Nom: Standard RWT rotor operating at nominal working conditions.

TC0: Standard RWT blade operating in a turbine without tilt and coning of the rotor.

TC0−Goff: Standard RWT blade operating in a turbine without tilt and coning of the rotor, Idem but switching gravity forces off.

Stiff: RWT turbine equipped with *hyper-stiff* blades operating at nominal conditions.

Stiff TC0: RWT with *hyper-stiff* blades without tilt and coning of the rotor.

Stiff T0: RWT with *hyper-stiff* blades without tilt, but with the standard coning of the rotor.

### 4.1. Analysis of aerodynamic effects

#### 4.1.1. Aerodynamic variables on the blade section

Fig. 6 shows the evolution of three representative aerodynamic variables along each turning cycle of the rotor. We focus our
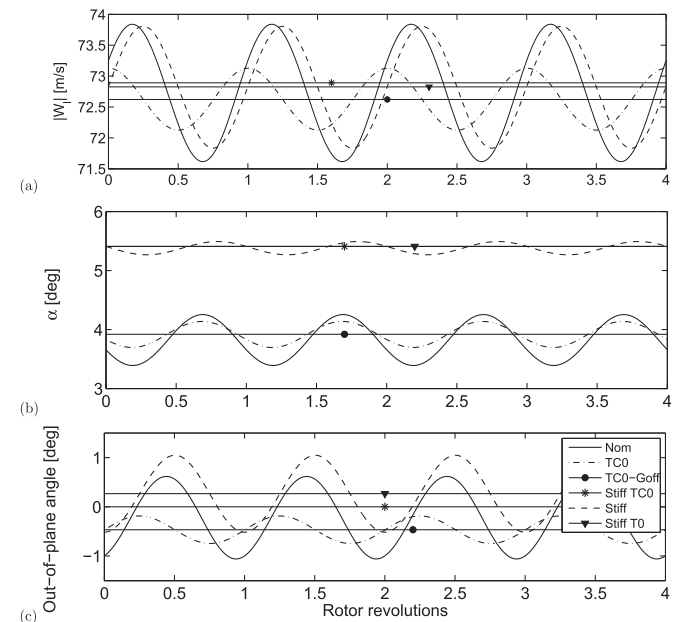


**Fig. 6.** Aerodynamic situation of blade # 1 at 90% of the span. Apparent wind magnitude (a), effective angle of attack (b), and out of plane angle (c) corresponding to a standard NREL 5 MW RWT.

analysis in a blade section located at 90% of the blade span, as representative of the aerodynamically-active part of the blade. Also, at this section near the tip of the blade structural deformation effects are intense enough to facilitate their observation, but aerodynamic tip effects are still small. Thus, it constitutes an ideal location to observe coupled aeroelastic phenomena. Results are plotted in function of the number of blade revolutions starting when the blade is in the vertical upper position. Due to the high aspect-ratio of the blades, the aerodynamics of the blade airfoil-sections is fairly two-dimensional. Thus, the aerodynamic forces depend mainly on the magnitude of the apparent wind $|\mathbf{W}_l|$ and angle of attack ($\alpha$). The evolution of these two variables is shown respectively in Fig. 6(a) and (b), under different hypothetical conditions. A third variable that has an additional influence, in terms of defining the aerodynamic forces on the airfoil section, is the span-wise component of the apparent wind, as, even when two-dimensional aerodynamics is considered, it reduces the projection of the apparent wind on the plane of the airfoil section ($W_{rel}$). In order to evaluate that, Fig. 6(c) shows the evolution of the out-of-plane angle of $\mathbf{W}_l$, OoP (as defined in Section 3), which is associated with the misalignment that takes $\mathbf{W}_l$ out of the plane of the airfoil section.

The magnitude of apparent wind velocity, $|\mathbf{W}_l|$, is a clear indicator of the aerodynamic interaction of the rotor with the wind free-stream and, as previously stated, has direct influence on the aerodynamic forces. For a given wind speed and turbine's rotational regime, fluctuations in the apparent-wind magnitude through the rotor indicate changes of interference in the axial direction, induction of tangential velocity, and additional velocity components due to blade vibration. Fig. 6(a) shows the time evolution of $|\mathbf{W}_l|$. We can start analyzing the curve for the **Stiff TC0** scenario which can be seen as a textbook base case. Here the apparent wind speed is constant during the rotor's turning cycle due to the symmetry of the aerodynamic configuration. The rotor does not have tilt nor cone, and their blades do not deform. For the next level of behavioral complexity, we can add two more alternative features to the reference **Stiff TC0** case. We can consider the effect of the rotor coning in case **Stiff T0**, where a slightly lower constant value of speed is seen, representing a higher level of interaction. Next, we can consider the effect of switching the tilt on in case **Stiff**, where the oscillatory behavior appears. The corresponding curve is perfectly centered around the one of the previous case, indicating that the only effect of tilt in this case is to introduce an asymmetry which adds an unsteady component on top of the stationary condition represented by the precedent case.

Another line of reasoning starting from the **Stiff TC0** scenario considers the effect of adding only the deformation of the blades, which gives the curve for the **TC0-Goff** scenario. Here, the difference from the previous case is a reduction in the magnitude of the apparent wind on the airfoil section, which again remains constant due to the constant deformation during the rotor's cycle. The higher misalignment of the airfoil section with respect to the undeformed configuration increases the level of interaction. In this scenario **TC0-Goff**, the interaction is higher than the corresponding to the **Stiff T0** case where the misalignment is only due to the coning of the rotor. If we add gravity effects to the previous case, the situation turns into scenario **TC0**, where the presence of gravity gives rise to an unsteady aerodynamic situation mainly triggered by oscillatory deformations that translate into geometry changes, and then, unsteady loading. The **TC0** curve is perfectly centered around the **TC0-Goff** one, indicating that in this case gravity only adds a fluctuating component. The addition of the two alternative lines of reasoning finally converge in the nominal scenario, which is identified as **Nom**. This case can be thought as a convolution of cases **Stiff** and **TC0** giving a higher oscillation amplitude which is smaller than the

sum of the previous cases. This has to do with the peaks of previous cases being uncorrelated, and thus partially cancelling each other. We can clearly identify the effect of gravity and tilt as independent sources of cyclic variations in the apparent wind. Fig. 7 shows a flowchart schematics summarizing the relation among the six hypothetical scenarios, and the two lines of reasoning followed during the analysis.

Following the same line of reasoning for the angle of attack (shown in Fig. 6(b)), we begin with the **Stiff TC0** scenario. Adding the rotor coning to it (moving into the **Stiff T0** scenario) does not significantly change the results, as both curves almost overlap. When tilt is added to the previous case, the oscillatory behavior appears; and the **Stiff** scenario curve again oscillates around the previous one. Following the alternative line of reasoning, the effect of deformation on the angle of attack can be clearly seen. Results for cases without blade deformation appear grouped in the upper part of the plot, and cases that consider deformation appear grouped in the lower part. Looking first purely at the effect of deformation, the **TC0-Goff** scenario shows a smaller angle of attack with respect to the base case, **Stiff TC0**. This is attributable to the effect of a coupling between twist and flapwise bending, in the blade deformational response, that would reduce the angle of attack as the blade bends. Again, gravity adds to the previous case a fluctuating component, which is centered around the **Stiff TC0** level curve, leading to the results for the **TC0** case. This fluctuation can also be attributed to a twist-bend coupling but in this case, connected with the fluctuating bending action of gravity, exerted mostly in the chord-wise direction. As it happened before with $|\mathbf{W}_l|$, the result for the nominal scenario is a combination of cases **Stiff** and **TC0**, with the amplitude being approximately the sum of both amplitudes, but with the phase mainly being imposed by the gravity loading. In this case, deformation clearly reduces the mean angle of attack. As stated in the discussion about the *square-cube law*, it can be foreseen that, as the typical blade length increases, the importance of gravity-driven fluctuations will be more significant than the bending-driven change of the angle of attack.

Fig. 6(c) shows that the out of plane angle behaves more likely to the apparent wind magnitude than to the angle of attack. This could be related with the fact that the change of this angle is connected to a change in misalignment of the chord-normal force with respect to the rotor's axis, affecting the axial induction factor. Comparing case **Stiff T0** with the base case **Stiff TC0**, it could be observed that, conversely to what happens with the angle of attack, the out of plane angle is heavily influenced by rotor coning. Additionally, the effect of blade deformation on the out of plane angle in case **TC0-Goff** is comparable to the effect of the rotor coning in magnitude, but in the opposite sense. This is consistent with the idea that the
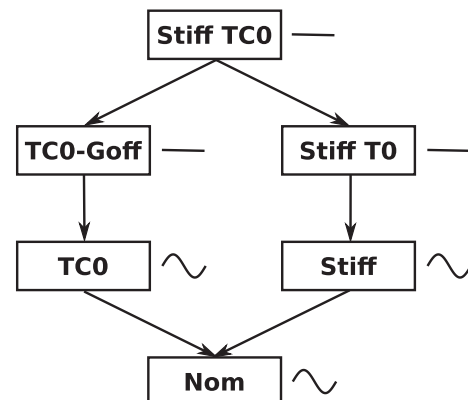


**Fig. 7.** Break down cases proposed to analyze sources of oscillating loads.

difference in angle of attack observed between cases with or without deformation can be attributed to twist-bending coupling more than to an aerodynamic effect. Later on, we shall investigate this further by analyzing pure structural-deformation variables. Again, following the previous two lines of reasoning, we get to the nominal scenario, which shows oscillations given by a composition of the effects of tilt and gravity-induced deformation.

### 4.1.2. Aerodynamic interference on the rotor plane

Fig. 8 shows the evolution of the angle between the incident wind and the rotor plane $\phi_{h_z}$ (see Section 3.2). The curves therein represent the effect of the aerodynamic interference both in the axial and the tangential directions, associated with the interference factors $a$ and $a'$ respectively (see Fig. 5(a)). Thus, $\phi_{h_z}$ constitutes another indicator of aerodynamic interaction, additional to the ones mentioned previously. It particularly indicates changes in the wind flow exerted by the rotor's presence, before any other velocity component (due either to structural vibration, or mechanical motion) is added to obtain the apparent wind. In this case, the rotor cone affects less significantly than the deformation due to the aerodynamic forces with respect to the base case. Another interesting effect revealed in this figure is that the peaks in the curve induced by gravity action (**TC0** scenario) occur when the blade is at a horizontal position, and are in the opposite sense than the peaks induced by tilt (**Stiff T0** scenario). As both these peaks are almost in phase, it results in a total oscillation amplitude smaller than in previous cases, diminishing the compound effect in the nominal scenario (**Nom**), which shows a small difference in phase that scarcely shifts the nominal curve. A remarkable aspect in Fig. 8 is that peaks from both tilt and gravity action are in phase, while in the apparent wind they are shifted by 1/4 rotor turn. This is closer to what happens with the angle of attack.

### 4.2. Analysis of structural response

#### 4.2.1. Blade deformation

Fig. 9 shows the evolution of two deformation measures: the out-of-rotor-plane displacement of the blade section, $U_{h_x}$, and its torsional rotation $\theta_{tor}$ (see Section 3.2) which has direct effect on the angle of attack. These deformation measures are useful to analyze the effect of dynamic geometrical changes on the rotor behavior. Here, we only show results for scenarios with the standard blade, as deformational measures for the *hyper-stiff* blade are practically nil. Starting with the first significant scenario, **TC0-Goff**, we can observe the flat curves corresponding to the constant values on both variables due to blade deformation induced by steady aerodynamic loads. When gravitational loads are added to the previous case (**TC0** scenario), oscillating displacement appears. As can be seen in Fig. 9(a), maximum and minimum values of $U_{h_x}$ approximately coincide with the blade being at upper and lower vertical positions of the turning cycle, indicating that the mayor source of displacement oscillations are gravity loads acting on the
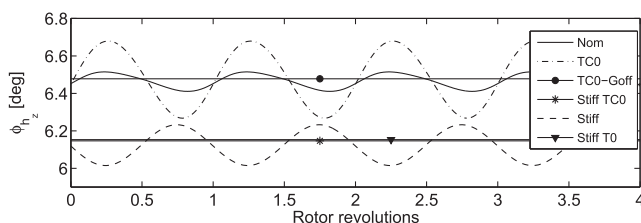
deformed blade, that project on the chord-normal direction, and produce out-of-plane bending, which alternatively adds and subtracts from the constant displacement produced by the steady aerodynamic loads. This also seems to be the cause of the oscillating behavior of the aerodynamic interaction revealed by the curve of apparent wind magnitude previously observed in Fig. 6(a). In the nominal scenario, as tilt and cone are introduced, a constant amount of displacement is added to the previous curves, which is produced by the rotor coning. Rotor tilt seems to have an almost imperceptible effect on $U_{h_x}$. This behavior seems consistent with the fact that, when the rotor has coning, blade deformation tends to increase the rotor's swept area, while when the rotor is plane (i.e. no coning), blade deformation tends to reduce swept area, implying less aerodynamic forces that deform the blades and a smaller displacement.

On the other hand, the maximum and minimum of the torsion angle curve in Fig. 9(b) coincide with the blade being at horizontal positions, indicating that the mayor player here is the gravity force acting chord-wise, which twists the blade through a bending-twist coupling. The torsion angle plot exhibits a flat curve corresponding to the **TC0-Goff** scenario, where all the torsion corresponds to deformation due to steady aerodynamic loads. The latter mostly produce bending, which clearly reveals the bending-torsion coupling. The **TC0** curve, which only differs in the presence of gravity, shows oscillation around the previous flat curve. This oscillation could only be originated by a coupling between torsion and bending in the rotor's plane, which is the prominent direction on which gravity loads act. Tilt and coning, considered in the nominal scenario has the effect of slightly increasing oscillation amplitude and mean value. The fact that the extrema of the previous plots do not exactly coincide with the vertical or horizontal positions of the blade reveals the aero-elasto-inertial coupled nature of the problem.

#### 4.2.2. Tower clearance

Fig. 10 shows the distance between the section at 90% of the span and the tower center. As a reference, the top tower diameter, as defined by Jonkman et al. [23], is 3.87 m, and the base diameter is 6 m, giving a diameter of around 5.24 m at the height at which the 90% section passes in front of the tower. The clearance is a limiting factor in the turbine design, guiding the choice of constructive features (like tilt, coning, and rotor overhang) in order to prevent a blade-tower collision. We chose the clearance as a significant factor, as it summarizes the effect of the rotor coning, tilt, constructive characteristics, and blade deformation due both to aerodynamic and gravity loading. Following the same line of reasoning as for previous magnitudes, we can start with the base case (**Stiff TC0**) to see that cone and blade deformation act in opposite ways in terms of this magnitude. Then, contribution from tilt (**Stiff** scenario) reveals to be much more significant than that of gravity effects (**TC0** case). Finally, this gives a curve for the nominal scenario similar to the former one with a constant shift given by blade deformation.

### 4.3. Fatigue effects

#### 4.3.1. Mechanical loads on the rotor hub

In order to analyze the effect of periodic loads on fatigue damage of critical turbine components, we selected three representative quantities that characterize the overall load condition on the rotor in terms of fatigue effects, namely: the torque on the shaft, and the bending moments at the blade root that produce bending in the rotor plane (*in-plane* bending) and normal to the rotor plane (*out-of-plane* bending) and the bending moments at blade root in the direction of rotation (*in-plane* bending) and in the turbine-axial
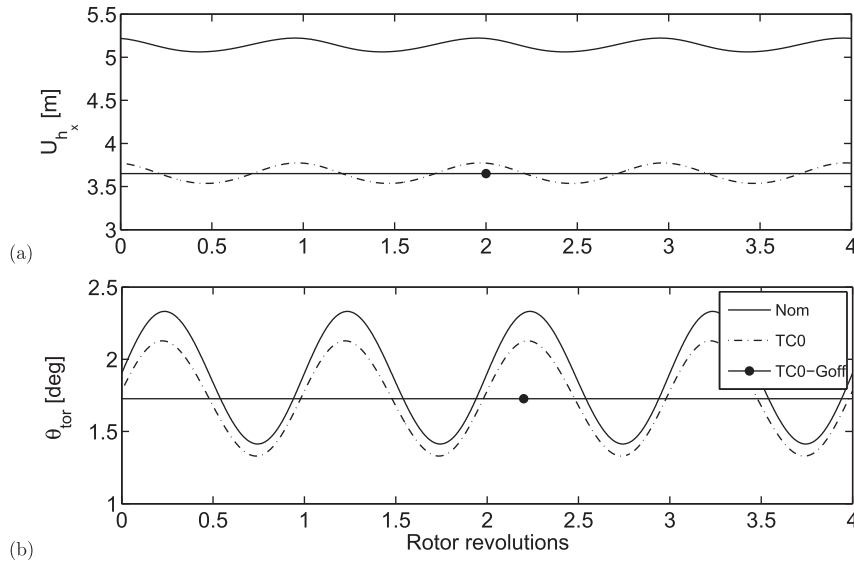


**Fig. 8.** Effect of rotor interference on the incident wind angle of blade # 1 at 90% of the span.

(a)

(b)

**Fig. 9.** Deformation measures of blade # 1 at 90% of the span. Out of rotor plane displacement $U_{h_x}$ (a) and torsional rotation angle $\theta_{tor}$ (b) corresponding to a standard NREL 5 MW RWT.
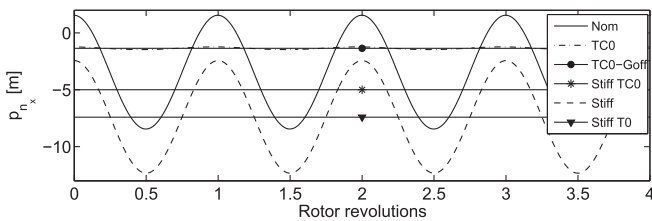


**Fig. 10.** Blade # 1 clearance from tower center $p_{n_x}$ at 90% of the span corresponding to a standard NREL 5 MW RWT.

direction (*out-of-plane* bending). Shaft shear stresses due to torque are proportional to the torque value and they reach their maximum on the external surface of the shaft. Stresses due to bending moments attain their maximum values at the points most distant from the blade root bending axis, and are proportional to the bending moment. Considering that the stresses relevant to fatigue analysis are proportional to the torque and bending moments, and given that our purpose is to compare different scenarios, we directly use those moments in our analysis of fatigue effects. We computed their mean value, their amplitude of oscillation, and their min/max ratio (*R*-value). The results for the six proposed scenarios are summarized in Table 1.

As it is expected from the well-balanced characteristics of a 3-blade rotor, shaft-torque amplitudes are negligible compared to their mean values in the proposed scenarios. This becomes clear by observing the shaft-torque amplitudes in Table 1 and their corresponding *R*-value. Wind turbine shafts are typically made of high-

tensile steel, which makes them less susceptible to the fatigue effects observed in the six scenarios proposed.

Results from blade root bending moments are more substantial. Out-of-plane moment amplitudes are around one tenth of the mean value in each case, except for the **TC0-Goff** scenario where loads are constant. Results for *hyper-stiff* blade configurations show a higher mean moment (in absolute value) but also a higher amplitude of oscillation. Rotor coning, comparing cases **Stiff TC0** and **Stiff T0**, increases the means value giving a lower *R*-value. Addition of tilt, in scenario **Stiff** increases both the mean and the amplitude giving the higher *R*-value.

The standard blade in scenario **TC0**, because of its elastic deformation, *absorbs* part of the load pulsation, considerably lowering the mean and amplitude, and producing a slight reduction in *R*-value compared with the **Stiff TC0** scenario (which is its analogous for the *hyper-stiff* blade). Finally, adding coning and tilt to get to the nominal configuration produces an increase in the mean, reflected in the lowest *R*-value. *R*-values for all cases, except **TC0-Goff**, range from 1.15 to 1.19.

The out-of-plane bending moment at the root could be used to further analyze fatigue effects on the blades. To this end, we turn to the Goodman diagram, which relates equivalent mean and amplitude values of stress for a given number of loading cycles. Mandell et al. [32] and Sutherland and Mandell [33] presented a detailed Goodman diagram for a typical fiberglass material used by the wind industry. Fig. 11 shows the curve corresponding to a high number of cycles ($10^8$) endurance highlighted in red. The curve has a slope of approximately 0.28 for *R* between 1.1 and 1.43 (marked as shaded

**Table 1**
Fatigue indicators computed from torque and blade root bending moments, in MNm, for the different turbine configurations.

| Case | Shaft torque | | | Out-of-plane bend moment | | | In-plane bend moment | | |
|---|---|---|---|---|---|---|---|---|---|
| | Mean | Amp | R | Mean | Amp | R | Mean | Amp | R |
| Stiff TC0 | 4.3482 | 0 | 1 | −10.029 | 0.8362 | 1.1819 | −0.9403 | 3.5326 | −1.7254 |
| Stiff T0 | 4.3374 | 0 | 1 | −10.861 | 0.8505 | 1.1699 | −1.1390 | 3.5329 | −1.9516 |
| TC0 Goff | 4.0892 | 0 | 1 | −8.184 | 0 | 1 | −0.5941 | 0 | 1 |
| Stiff | 4.2958 | $0.35 \cdot 10^{-3}$ | 0.9998 | −11.123 | 0.9775 | 1.1927 | −1.2151 | 3.4705 | −2.0776 |
| TC0 | 4.0878 | $0.65 \cdot 10^{-3}$ | 0.9997 | −8.175 | 0.6641 | 1.1768 | −0.5940 | 3.6761 | −1.3855 |
| Nom | 4.0487 | $1.10 \cdot 10^{-3}$ | 0.9995 | −9.164 | 0.6576 | 1.1546 | −0.8388 | 3.6256 | −1.6020 |
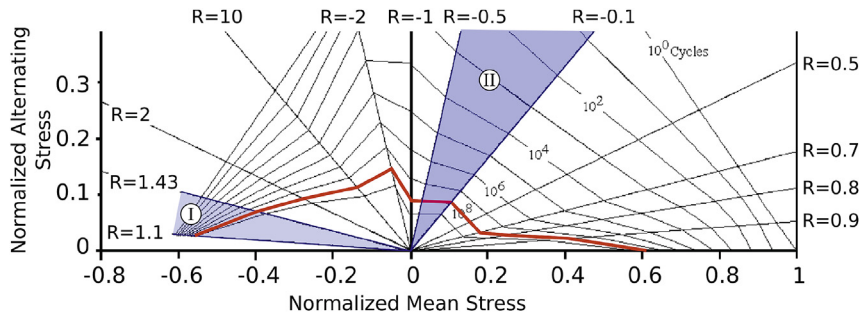
**Fig. 11.** Goodman diagram modified from Mandell et al. [32]. Curve for $10^8$ cycles is highlighted.

region I in the figure). Assuming that the standard blade was designed safely in terms of fatigue resistance, we can compare the locus for the six different scenarios in that portion of the Goodman diagram. These are shown in Fig. 12(a). A line passing through the locus for the nominal scenario with the 0.28 slope will separate cases with better fatigue expectation than the nominal, those below that line, from cases with worse fatigue expectation lying above that line. Following this line of reasoning, it can be seen that scenarios with the *hyper-stiff* blade present worse fatigue behavior than the nominal case, regardless of any other conditions. This could support the adoption of softer blades when designing future wind turbines. In both cases, tilt and cone tend to worsen the situation, resulting in a compromise between ensuring tower clearance and improving fatigue behavior.

Regarding the in-plane blade root moment, Table 1 shows very similar amplitude values for all the proposed cases. The conclusions for the in-plane moment are similar than for the out-of-plane moment, as the positions relative to the nominal case are qualitatively the same.

### 4.3.2. Loads on the blade section

We also analyzed the effect of different configurations on bending moments at a particular blade section to characterize their structural effect. We chose the section at 90% of the blade span as in the previous analysis. This selection is consistent with the findings of Liu et al. [34] who found that, when blade vibration is considered, a significant aerodynamic fatigue load increase is found near blade tip, which reduces towards rotor axis. This increase is still a 6% at 75% rotor radius, with significant reduction of the aerodynamic fatigue loads per unit length in the out-of-plane and in-plane directions respectively. Authors also found that blade vibration has great influence on the out-of-plane damage equivalent

bending moment, especially for the outer part of the blade. The impact decreases towards the blade root, with still a 4.5% increase at 5% rotor radius. In Table 2, we present the mean value, the amplitude of oscillation, and the $R$-value of bending moment components in that section in both, the chord-normal and the chord-wise directions, for the six different scenarios.

$R$-values for the chord-normal component are very close to 1, so we could repeat the procedure with the Goodman diagram, in this case shown in Fig. 12(b). From Fig. 11 we obtain the same slope for $R$-values near 1.1 and $10^8$ cycles that we got in the previous case: approximately 0.28. From Fig. 12(b), it can be seen that the fatigue situation of all the cases arrange in a similar pattern than in the case of the out-of-plane blade root moment, with the exception that this time case **TC0** lies on the line passing through the nominal case. The chord-wise component in Table 2 has $R$-values that lie in the $-0.5 < R < 0.1$ region of the Goodman diagram (shaded region II in Fig. 11), where the line for $10^8$ cycles is horizontal. Thus, the fatigue condition can be analyzed in terms of the amplitude. In this case, the lower amplitude results from the nominal scenario with the **TC0** case giving higher values. The same is found for the scenarios

**Table 2**
Fatigue indicators computed from blade bending moments, in kNm, at 90% blade length for the different turbine configurations.

| Case | Chord-normal bend moment | | | Chord-wise bend moment | | |
|---|---|---|---|---|---|---|
| | Mean | Amp | R | Mean | Amp | R |
| Stiff TC0 | −88.174 | 0.1973 | 1.0045 | 9.0312 | 9.2308 | −0.01093 |
| Stiff T0 | −92.001 | 0.5728 | 1.0125 | 8.9644 | 9.2308 | −0.01464 |
| TC0 Goff | −55.719 | 0 | 1 | 5.2552 | 0 | 1 |
| Stiff | −92.603 | 1.8111 | 1.0399 | 8.9041 | 9.220 | −0.01743 |
| TC0 | −55.784 | 2.7685 | 1.1044 | 5.2587 | 9.0509 | −0.26501 |
| Nom | −58.334 | 2.1308 | 1.0758 | 4.8697 | 8.7628 | −0.28557 |
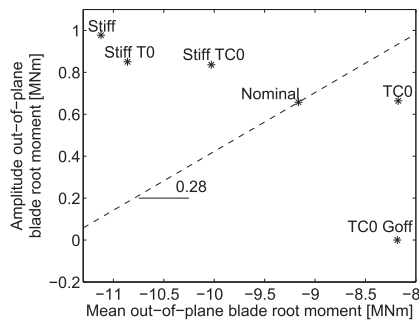


(a)
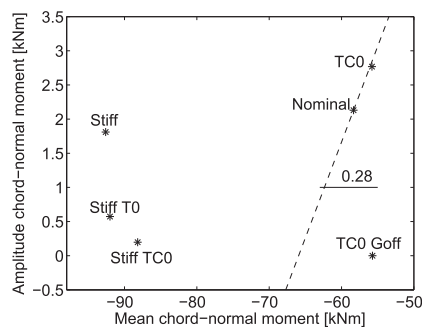


(b)

**Fig. 12.** Partial Goodman diagram for the out-of-plane blade root bending moment (a) and the chord-normal bending moment at 90% blade length (b) showing the situation against combined fatigue of the analyzed cases.
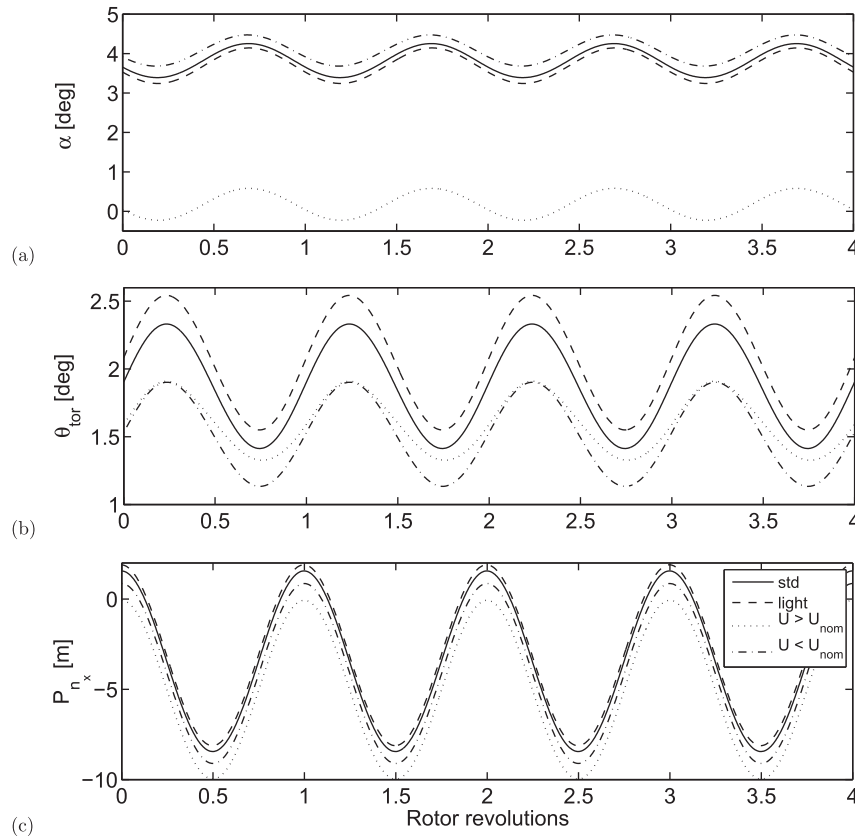
**Fig. 13.** Comparison of different variables under different situations for blade # 1 at 90% of the span. Angle of attack (a), torsional rotation angle (b), and section clearance from tower center (c) comparing a standard NREL 5 MW RWT versus the *light blade* presented before and nominal wind with lower and higher wind speeds.

using the *hyper-stiff* blade, which give higher amplitude values, with cases **Stiff TC0** and **Stiff T0** showing higher amplitudes than the **Stiff** case, which includes both tilt and cone. The large amplitude value in this component is a reflection of the action of gravity forces, which have a higher projection in the chord-wise direction.

## 5. Conclusions

In this work we have analyzed the sources of periodic loads on horizontal axis wind turbines with emphasis in the future scaling needs of the industry. We deconstructed the problem by the introduction of six hypothetical configurations defining scenarios which highlight the effect of different sources. This analysis could only be possible thanks to the rich phenomena description attained by the aero-elasto-inertial code used, described in Section 3.1. Apart from a detailed representation of aerodynamic phenomena it is able to adequately represent the effect of different ways of coupling bending in two directions and torsion. In this qualitative study we focused on understanding how different design parameters produce cyclic loads and which impact they will have in future scaled turbines.

We started by analyzing the evolution of aerodynamic variables (apparent wind magnitude, angle of attack and out of plane angle) in each of the test-case scenarios. One conclusion drawn at this step is that coning angle affects mainly the out-of-plane angle but its effect on the angle of attack is negligible. Next, we studied the effect of different configurations on energy extraction by analyzing the rotor interference. Results show that interference is more related to the angle of attack than to other aerodynamic variables. After that, we turned into structural variables selecting the two more relevant

to the phenomena under study, blade out-of-plane displacement and torsional deformation. In this case, gravity loads are identified as a mayor source of displacement oscillations producing out of plane bending which relates to the observed interference behavior, and torsional oscillations activated by twist coupled with in-plane bending. This gravity-induced oscillations, which would become more significant in future up-scaled machines due to the square-cube law, could be controlled by adjusting the amount of bend-twist coupling. It is interesting to note here that Cox and Echtermeyer [35] found that bend-twist coupling is independent of geometric scaling, but the magnitude of displacement will increase with blade length. Again this kind of behavior could not be revealed without the descriptive capabilities of our model. Then, we studied the tower clearance as a summarizing factor of the aero-elasto-inertial dynamics, as it clearly reveals the effect of coning, tilt, and other constructive characteristics, in combination with blade deformation due both to aerodynamic and gravity loads. It has been seen how coning and blade deformation act in opposite ways, and that contribution from tilt is much more significant than that of gravity effects. In this regard, the only way of reducing tilt activated oscillations is to eliminate or, at least, reduce the need of tilt. This could be achieved by means of downwind rotors with the penalty of increased effects due to tower interference. Other way of reducing tilt would be to increase rotor coning, but as blades become more flexible, coning would need to be greatly increased resulting in big differences between unloaded and loaded configurations. Also, it can be foreseen that, as the blade length increase, the importance of gravity-induced fluctuations will be more significant than the bending-induced fluctuations of the angle of attack.

Finally, we analyzed how the different sources of periodic loading affect the fatigue behavior. We analyzed both global quantities such as shaft torque and blade root moments, and local quantities such as blade section bending moments. We found out that the shaft torque is almost insensitive to this kind of loads and is practically not affected by the different scenarios although the nominal case is the one with the greater oscillating component. Regarding blade root bending moments, the out-of-plane moment show *R*-values ranging from 1.15 to 1.19 given by a fluctuating component about one tenth of the mean value, while the in-plane moment has *R*-values near −2 corresponding to fluctuating components more than three times the mean. From all the configurations, those with *hyper-stiff* blades exhibit the worst fatigue behavior compared with those with the standard blade. Also, it is found that tilt and coning generally worsen fatigue behavior. Blade section moments show qualitatively similar features than blade root moments. In this case, the relation between the chord-normal moment amplitude and its mean is much smaller than a tenth. Mean and amplitude of the chord-wise moment are of the same order of magnitude, revealing a strong dependency with gravity-induced loading. From the latter, we can infer that flexibility improves fatigue behavior while tilt and coning worsen it.

The use of *hyper-stiff* blades served here as a theoretical artifact to study different phenomena by means of deconstructing the rotor aeroelastic behavior by ruling out the structural deformation and the feedback between structural and aerodynamic variables separating both aspects of the coupled problem. Comparing results for cases with *hyper-stiff* and standard blades could give an idea of the information missing by disregarding deformation.

As a way to check that our analysis can be extrapolated to other load conditions and future ULB rotors, Fig. 13 shows a comparison between the standard and a hypothetical *light* blade working under nominal conditions, and the standard blade working at wind speeds lower and higher than the nominal. We selected three magnitudes representative of the aerodynamic, structural and global behavior of the blades. It can be seen that the four curves behave qualitatively in the same way, allowing to extend the findings of this work to lighter blades and different wind regimes.

As an outlook for further work, we plan to focus our research efforts on load dynamics related with unsteady wind, and its effect on wind turbines in relation with different constructive and operational features. Unsteady-wind related loads are usually non periodic, although they could be cyclic, and may be stochastic. Loads resulting from atmospheric boundary layer velocity profile, tower shadow interference and turbulence, combined with different constructive features, need to be analyzed with the perspective of future turbine upscaling in mind.

## Acknowledgments

## References

[1] N. Dimitrov, A. Natarajan, J. Mann, Effects of normal and extreme turbulence spectral parameters on wind turbine loads, Renew. Energy 101 (Supplement C) (2017) 1180–1193.
[2] X. Liu, C. Lu, S. Liang, A. Godbole, Y. Chen, Vibration-induced aerodynamic loads on large horizontal axis wind turbine blades, Appl. Energy 185 (Part 2) (2017) 1109–1119.
[3] X. Cai, R. Gu, P. Pan, J. Zhu, Unsteady aerodynamics simulation of a full-scale horizontal axis wind turbine using cfd methodology, Energy Convers. Manag. 112 (Supplement C) (2016) 146–156.
[4] A.M. AbdelSalam, V. Ramalingam, Wake prediction of horizontal-axis wind turbine using full-rotor modeling, J. Wind Eng. Ind. Aerod. 124 (Supplement C) (2014) 7–19.
[5] M. Talavera, F. Shu, Experimental study of turbulence intensity influence on wind turbine performance and wake recovery in a low-speed wind tunnel, Renew. Energy 109 (Supplement C) (2017) 363–371.
[6] G. Bir, J. Jonkman, Aeroelastic instabilities of large offshore and onshore wind turbines, J. Phys. Conf. Ser. 75 (1) (2007), 012069.
[7] J. Holierhoek, An overview of possible aeroelastic instabilities for wind turbine blades, Wind Eng. 37 (4) (2013) 421–440.
[8] D.T. Griffith, T.D. Ashwill, The Sandia 100-meter All-glass Baseline Wind Turbine Blade: SNL100-00, Report SAND2011–3779, Sandia National Laboratories, 2011.
[9] D.T. Griffith, The SNL100–S101 Blade: Carbon Design Studies for the Sandia 100-meter Blade, Report SAND2013-1178, Sandia National Laboratories, 2013.
[10] D.T. Griffith, The SNL100–S102 Blade: Advanced Core Material Design Studies for the Sandia 100-meter Blade, Report SAND2013-10162, Sandia National Laboratories, 2013.
[11] M. Hansen, Aerodynamics of Wind Turbines, Routledge/Earthscan, 2015.
[12] P. Ragan, L. Manuel, Comparing estimates of wind turbine fatigue loads using time-domain and spectral methods, Wind Eng. 31 (2) (2007) 83–99.
[13] D.S. Zalkind, L.Y. Pao, The fatigue loading effects of yaw control for wind plants, in: American Control Conference (ACC), 2016, IEEE, 2016, pp. 537–542.
[14] T. Kim, A.M. Hansen, K. Branner, Development of an anisotropic beam finite element for composite wind turbine blades in multibody system, Renew. Energy 59 (Supplement C) (2013) 172–183.
[15] J. O'Brien, T. Young, D. O'Mahoney, P. Griffin, Horizontal axis wind turbine research: a review of commercial CFD, FE codes and experimental practices, Prog. Aerosp. Sci. 92 (Supplement C) (2017) 1–24.
[16] C. Gebhardt, B. Roccia, Non-linear aeroelasticity: an approach to compute the response of three-blade large-scale horizontal-axis wind turbines, Renew. Energy 66 (Supplement C) (2014) 495–514.
[17] W. Mo, D. Li, X. Wang, C. Zhong, Aeroelastic coupling analysis of the flexible blade of a wind turbine, Energy 89 (2015) 1001–1009.
[18] L. Wang, X. Liu, N. Renevier, M. Stables, G.M. Hall, Nonlinear aeroelastic modelling for wind turbine blades based on blade element momentum theory and geometrically exact beam theory, Energy 76 (2014) 487–501.
[19] D. Malcolm, A. Hansen, Windpact Turbine Rotor Design Study: June 2000–june 2002 (Revised), Tech. Rep., National Renewable Energy Laboratory (NREL), Golden, CO, 2006.
[20] J.M. Jonkman, M.L. Buhl Jr., Fast User's Guide, Tech. Rep. NREL/EL-500–38230, National Renewable Energy Laboratory (NREL), Golden, Colorado, USA, 2005.
[21] H. Meng, F.S. Lien, L. Li, Elastic actuator line modelling for wake-induced fatigue analysis of horizontal axis wind turbine blade, Renew. Energy 116 (Part A) (2018) 423–437.
[22] J.F. Manwell, J.G. McGowan, A.L. Rogers, Wind Energy Explained: theory, Design and Application, Wiley, Chichester, UK, 2002.
[23] J. Jonkman, S. Butterfield, W. Musial, G. Scott, Definition of a 5-MW Reference Wind Turbine for Offshore System Development, Tech. Rep. NREL/TP-500–38060, National Renewable Energy Laboratory, 2009.
[24] F.L. Ponta, A.D. Otero, L.I. Lago, A. Rajan, Effects of rotor deformation in wind-turbine performance: the dynamic rotor deformation blade element momentum model (DRD-BEM), Renew. Energy 92 (2016) 157–170.
[25] A.D. Otero, F.L. Ponta, Structural analysis of wind-turbine blades by a generalized Timoshenko beam model, J. Sol. Energy Eng. 132 (1) (2010) 011015.
[26] A.D. Otero, F.L. Ponta, L.I. Lago, Structural analysis of complex wind turbine blades: flexo-torsional vibrational modes, in: R. Carriveau (Ed.), Advances in Wind Power, InTech, 2012, pp. 123–149.
[27] L.I. Lago, F.L. Ponta, A.D. Otero, Analysis of alternative adaptive geometrical configurations for the NREL-5 MW wind turbine blade, Renew. Energy 59 (2013) 13–22.
[28] P. Zhang, S. Huang, Review of aeroelasticity for wind turbine: current status, research focus and future perspectives, Front. Energy 5 (4) (2011) 419–434.
[29] Q. Wang, M.A. Sprague, J. Jonkman, N. Johnson, B. Jonkman, Beamdyn: a high-fidelity wind turbine blade solver in the fast modular framework, Wind Energy 20 (8) (2017) 1439–1462.
[30] P. Moriarty, A. Hansen, W. Aerodyn Theory Manual (US), N.R.E.L., Engineering, National Renewable Energy Laboratory, 2005.
[31] D. Laino, A. Hansen, User's Guide to the Wind Turbine Aerodynamics Computer Software Aerodyn, Tech. Rep., National Renewable Energy Laboratory, 2002. under subcontract No. TCX-9-29209-01
[32] J. Mandell, D. Samborsky, N. Wahl, H. Sutherland, Testing and analysis of low cost composite materials under spectrum loading and high cycle fatigue conditions, in: 14th International Conference on Composite Materials: Technical Session Proceedings, 2003, p. 1811.
[33] H.J. Sutherland, J.F. Mandell, The effect of mean stress on damage predictions for spectral loading of fibreglass composite coupons, Wind Energy 8 (1) (2005) 93–108.
[34] X. Liu, C. Lu, S. Liang, A. Godbole, Y. Chen, Vibration-induced aerodynamic loads on large horizontal axis wind turbine blades, Appl. Energy 185 (Part 2) (2017) 1109–1119. Clean, Efficient and Affordable Energy for a Sustainable Future.
[35] K. Cox, A. Echtermeyer, Geometric scaling effects of bend-twist coupling in rotor blades, Energy Procedia 35 (2013) 2–11.